

# Dynamic slab segmentation due to brittle-ductile damage interactions in the outer rise

Taras Gerya (✉ [taras.gerya@erdw.ethz.ch](mailto:taras.gerya@erdw.ethz.ch))

ETH-Zurich <https://orcid.org/0000-0002-1062-2722>

David Bercovici

Yale University

Thorsten Becker

The University of Texas <https://orcid.org/0000-0002-5656-4564>

---

## Physical Sciences - Article

**Keywords:** Oceanic Plate Recycling, Thermo-clinical Evolution, Subduction Trenches, Bending Memory

**Posted Date:** November 30th, 2020

**DOI:** <https://doi.org/10.21203/rs.3.rs-85800/v1>

**License:** © ⓘ This work is licensed under a Creative Commons Attribution 4.0 International License.

[Read Full License](#)

---

**Version of Record:** A version of this preprint was published at Nature on November 10th, 2021. See the published version at <https://doi.org/10.1038/s41586-021-03937-x>.

1 **Dynamic slab segmentation due to brittle-ductile damage interactions in the**  
2 **outer rise**

3

4 T. V. Gerya<sup>1</sup>, D. Bercovici<sup>2</sup> & T. W. Becker<sup>3,4</sup>

5 <sup>1</sup>Swiss Federal Institute of Technology Zurich, Department of Earth Sciences, Zurich,  
6 Switzerland.

7 <sup>2</sup>Yale University, Earth & Planetary Science, New Haven, CT, United States

8 <sup>3</sup>Institute for Geophysics, Jackson School of Geosciences, The University of Texas at  
9 Austin, Austin, TX, United States

10 <sup>4</sup>Department of Geological Sciences, Jackson School of Geosciences, The University of  
11 Texas at Austin, Austin, TX, United States

12

13

14

15 **The recycling of oceanic plates by means of subduction represents the major**  
16 **plate driving force and subducting plate strength controls many aspects of the**  
17 **thermo-chemical evolution of Earth. Regardless of its prior history, each**  
18 **subducting plate experiences intense normal faulting<sup>1-11</sup> during bending that**  
19 **accommodates the transition from horizontal to downward motion at the**  
20 **outer rise at subduction trenches. Here, we investigate the consequences of**  
21 **this bending-induced plate damage using new numerical, thermomechanical**  
22 **subduction models in which both brittle and ductile deformation, as well as**  
23 **grain size evolution, are tracked and coupled self-consistently. Pervasive slab**  
24 **weakening and pronounced segmentation can occur at the outer rise region**  
25 **due to the strong feedback between brittle and ductile damage localization.**  
26 **The “memory” of bending varies from segmentation to broadly-distributed**  
27 **damage depending on the age of the subducting plate, mantle potential**  
28 **temperature, and the magnitude of strain-induced weakening of outer rise**  
29 **normal faults. This new slab damage phenomenon explains the development**

30 **of large-offset normal faults<sup>8,9</sup>, the occurrence of deep compressional thrust-**  
31 **faulting earthquakes<sup>12</sup>, and the appearance of localized areas of reduced**  
32 **effective viscosity<sup>13</sup> observed at subduction trenches. Furthermore, brittle-**  
33 **viscously damaged slabs show a strong tendency for slab breakoff at elevated**  
34 **mantle temperatures. Given Earth's planetary cooling history<sup>14</sup>, this implies**  
35 **that intermittent subduction with frequent slab breakoff episodes<sup>15,16</sup> may**  
36 **have been characteristic for terrestrial plate tectonics until more recent times**  
37 **than expected from memory-free rheologies<sup>17</sup>.**

38  
39 Subduction of negatively buoyant oceanic lithosphere is a key driver of terrestrial  
40 tectonics. Subduction results from buoyancy forces that bend and pull the  
41 lithosphere into the interior of the Earth's mantle where mechanical properties of  
42 subducted lithospheric slabs are strongly modified by various physical-chemical  
43 processes<sup>18-20</sup>. One of the large-scale effects of this modification is the pronounced  
44 mechanical dichotomy of stronger lithospheric plates at the surface and weaker  
45 slabs in the Earth's interior that has been proposed on the basis of various  
46 geological-geophysical data combined with numerical modeling<sup>20-22</sup>. Whereas strong  
47 plates at the surface are a pre-requisite for terrestrial style one-sided  
48 subduction<sup>15,20,23</sup> weakened lithospheric subducted slabs, which pile, bend, segment  
49 or lie flat at the top of the lower mantle, are needed to reproduce the spectrum of  
50 slab morphologies observed on Earth<sup>24,25</sup> as well as the observed variations of the  
51 Earth's geoid<sup>18,26</sup>. Slab weakening seems in apparent contradiction with  
52 experimentally calibrated, thermally activated rheological laws for the lithospheric  
53 mantle<sup>27,28</sup>, which predict high effective viscosity ( $> 10^{24}$  Pa s) of subducted slabs in  
54 the upper mantle<sup>18,29</sup>, implying a slab/mantle viscosity contrast of  $\gg 1000$ . In  
55 contrast, a number of observations, combined with modeling studies, suggest that  
56 this contrast should be much lower (of the order of 100)<sup>19,22,24,30</sup>, for example to  
57 reconcile the dynamics with seismic tomography models that indicate strong  
58 deformation and even disruption of subducted slabs in the upper mantle<sup>24,25,31</sup>.

59 The apparent rheological paradox of strong plates and weak slabs<sup>20,24</sup> can be  
60 resolved by assuming some additional lithospheric weakening processes that are

61 intrinsically related to the transition from horizontal plate motion to its diving into  
62 the mantle. In this respect, plate bending at the outer rise is a primary candidate for  
63 changing the mechanical properties of the lithosphere<sup>5,6,19</sup>. Each subducting plate,  
64 irrespective of its age and earlier history, unavoidably experiences a transition from  
65 its horizontal to vertical motion through bending when passing through the outer  
66 rise region that is present at every subduction trench. Plate bending is not fully  
67 elastic and is associated with a number of irreversible physical-chemical processes  
68 that can profoundly change the mechanical properties of the subducting plate<sup>1,5,8-  
69 10,19</sup>. As the result, the elastic strength of the plate is completely lost within 100 km  
70 of the trench axis through faulting and ductile deformation. This requires that  
71 coupling of the slab to the plate occurs through viscous stresses, making the trench  
72 topography a dynamic feature<sup>19</sup>.

73         It is well understood that the colder, brittle top region of subducting plates is  
74 pervasively damaged by extensional outer rise normal faulting<sup>1,4,9,11,19</sup>, possibly  
75 associated with downward water penetration and mantle lithosphere  
76 serpentinization<sup>2,3,5-7,10</sup>. In contrast, the deeper and warmer portions of the plate  
77 deform in compression by viscous creep<sup>13,32</sup> and can potentially be affected by  
78 ductile damage processes such as grain size reduction assisted by Zener pinning<sup>33-38</sup>.  
79 Relating these brittle and ductile damage processes to the plate bending at the outer  
80 rise can advance our understanding of whether and how the pervasive weakening of  
81 subducting plates may occur in nature and what consequences that deformation  
82 memory will have for the dynamics and stability of subduction.

83         Here, we investigate the consequences of bending-induced plate damage by  
84 using new 2D numerical thermomechanical subduction models in which both  
85 brittle-plastic and ductile deformation as well as grain size reduction and growth  
86 are coupled self-consistently (Methods). Our modeling results indicate that brittle-  
87 ductile slab weakening and plate segmentation should occur at the outer rise region  
88 due to the strong feedback between brittle and ductile damage localization.

89  
90  
91

92           **Slab segmentation by bending at the outer rise**

93           Figure 1 shows an example of a typical model evolution resulting in  
94           subducting slab damage and segmentation. The numerical experiment starts from  
95           subduction initiation at a transform fault<sup>23,39</sup> which separates two oceanic plates of  
96           different ages, leading to lateral gravitational instability. The older plate starts to  
97           subduct in a retreating manner whereas the younger, now overriding plate is  
98           subjected to extension and horizontal motion toward the retreating trench. After the  
99           initial period of retreat associated with gradual downward sinking and steepening  
100           of the slab, the slab angle stabilizes and the advancing horizontal motion of the  
101           subducting plate begins. This mode of subduction continues until the slab reaches  
102           the mantle transition zone and starts to flatten due to the negative Clapeyron slope  
103           of the spinel-perovskite phase transition (Methods), which initiates a new episode  
104           of trench retreat. The viscosity of the subducting plate that results from this  
105           dynamically self-consistent subduction scenario shows a pattern of 150-200 km  
106           long segments separated by narrow low-viscosity zones. This damage pattern forms  
107           as the result of linked, localized brittle-plastic deformation and grain-size reduction  
108           at the outer rise (Fig. 2a, b). As a consequence, the subducting slab deforms easily in  
109           a chain-like fashion in response to its interaction with the mantle transition zone.  
110           The resulting slab morphologies are markedly different from those of visco-plastic  
111           slabs without damage<sup>22,24</sup> and reflect the influence of the strong coupling between  
112           the brittle and ductile strain localization mechanisms during plate bending.

113           Model sensitivity studies show that the style of slab deformation depends  
114           strongly on both the ductile damage and the strain-induced weakening of faults as  
115           well as on the age of the subducting plate and the mantle potential temperature. In  
116           particular, deactivation of ductile damage (grainsize reduction) and/or strain-  
117           induced weakening produces smoothly bent slabs (cf. Fig. 3a and b, c, d) comparable  
118           to previous subduction models<sup>15,23,24</sup>. Lack of ductile damage also makes subduction  
119           initiation more difficult (cf. Figs. 4a and c) due to the increased bending resistance of  
120           the subducting plate. The combined effects of fault weakening and ductile damage  
121           on slab segmentation are notably distinct from the individual forms of weakening. In  
122           the absence of normal fault weakening, slab segments disappear and grain size

123 reduction inside the subducting plate is distributed more evenly (cf. Figs. 3a and c).  
124 This, in turn, causes distributed rather than localized, segmented weakening of  
125 slabs. A similar effect is achieved by decreasing the rate of fault-weakening with  
126 strain (cf. Figs. 4b and c). In contrast, in the absence of ductile damage, slab  
127 segments remain but the displacement along individual normal faults reduces and  
128 consequently the large-offset normal faults disappear (cf. Fig. 3b). As a result, the  
129 number of segments increases together with a decrease in the characteristic  
130 segment length (cf. Figs. 3a and b). The total amount of deformation in each segment  
131 also decreases. Slab segmentation is thus primarily driven by normal fault  
132 weakening whereas the ductile damage makes this process more intense, localized  
133 and laterally extensive. Ductile creep of mature faults has no influence on  
134 segmentation and mainly affects the deformation of segmented slabs in the mantle:  
135 weaker (serpentine type) rheology facilitates slab bending and breakoff whereas  
136 stronger (dry olivine type) rheology produces less deformed slabs (Extended Data  
137 Table 2).

138         The age of the subducting plate also controls the characteristic length of slab  
139 segments: older and thus thicker subducting plates show longer slab segments, but  
140 become much shorter in younger plates (cf. Figs. 4c and d). An increase in the  
141 mantle potential temperature, in contrast, promotes slab segmentation and bending  
142 by steepening of the slab angles due to the reduced amount of viscous resistance of  
143 the asthenosphere to slab penetration (cf. Figs. 1 and 3a, 5a). This also leads to  
144 notable acceleration of subduction and more frequent slab breakoff<sup>15,16</sup> (cf. Figs. 1  
145 and 3a, 5a).

#### 146         **Why should outer rise faults weaken with strain?**

147         Our numerical models suggest that strain weakening of outer rise normal  
148 faults is a key process controlling subducting slab segmentation, and is thus  
149 discussed further. Strain weakening of faults is a common assumption of  
150 geodynamic models<sup>40</sup> and is crucial for reproducing a number of strain localization  
151 phenomena in both oceanic and continental lithosphere such as large-offset normal  
152 faults<sup>40</sup>, oceanic transform faults<sup>41</sup>, oceanic and continental core complexes<sup>42</sup>. The  
153 physics of this process is incompletely understood and may include (but is not

154 limited to) pressurized fluid percolation<sup>23</sup>, growth of hydrous minerals<sup>43</sup>, structural  
155 softening<sup>44</sup>, shear heating<sup>45</sup>, coseismic weakening and grain size reduction<sup>46</sup>,  
156 intergranular cavitation<sup>47</sup>. Intense hydration of outer rise normal faults has been  
157 suggested on the basis of seismological, geophysical and theoretical arguments<sup>2,3,5-</sup>  
158 <sup>7,10,12</sup>.

159 In particular, numerical models<sup>5,48</sup> find that the dynamic pressure associated  
160 with plate bending may be large enough to overcome the confining lithostatic  
161 pressure and cause downward water suction along outer rise normal faults. In  
162 contrast, analytical models<sup>11</sup> suggests that such large dynamic pressure cannot be  
163 achieved, and lowered seismic velocities within the oceanic lithosphere under the  
164 outer rise may instead be explained by thermal cracking. Such uncertainties  
165 regarding the extent of outer rise fault hydration aside, it is clear that these  
166 structures systematically reveal lowered friction coefficients ( $\leq 0.3$ )<sup>12</sup> compared to  
167 dry oceanic lithosphere (0.6-0.85)<sup>49,50</sup>, and only such as overall weakening is what is  
168 required for our simplified strain weakening models (Methods).

169

### 170 **Evidence for segmentation of subducting slabs in nature**

171 One of the testable consequences of the emergent phenomena of slab  
172 segmentation is the development of large-offset normal faults localized above the  
173 regions of intense grain size reduction. Like the deep slab morphology, this  
174 heterogeneous faulting pattern contrasts with broadly distributed, smaller-offset  
175 normal faults as produced by models without grain size reduction<sup>4-6</sup>. Large offset  
176 normal faults are indeed observed at some subduction trenches, such as in Japan  
177 trench, based on geological-geophysical observations<sup>8,9</sup>. Intriguingly, the deeper  
178 parts of the subducting plate in Japan have been inferred to display a localized area  
179 of reduced effective viscosity based on post-seismic deformation<sup>13</sup>. This zone of  
180 weakening may correspond to the areas of grainsize reduction that systematically  
181 develop in our models in either strongly localized (Fig. 4c) or more widely  
182 distributed (Fig. 4b) manner.

183           Moreover, global slab seismicity in the outer rise is often characterized by the  
184 presence of deep (20-50 km) compressional, thrust-faulting earthquakes. These  
185 earthquakes often occur below the elastic core of the subducting plate at the  
186 temperatures up to 600°C<sup>12</sup>, i.e., close to the brittle-ductile transition in the mantle  
187 lithosphere. The flow-to-friction transition near the base of the seismogenic zone  
188 may be characterized by a runaway transition from dislocation and diffusion creep  
189 to dilatant deformation, involving incompletely accommodated grain boundary  
190 sliding<sup>47</sup>. Localization of the compressional ductile deformation observed in our  
191 numerical experiments (Fig. 2 a,b) and controlled by grain size reduction may thus  
192 create favorable conditions for deep thrust-faulting. In the coldest parts of these  
193 localized ductile deformation zones, dislocation and diffusion creep may become too  
194 slow to accommodate the increasing shear strain rate, leading to intergranular  
195 cavitation, weakening, strain localization, and a switch from stable flow to runaway  
196 fault rupture<sup>47</sup>.

197

### 198           **Slab segmentation and occurrence of intermittent subduction**

199           Besides explaining these subduction zone features, the emergent  
200 phenomenon of brittle-ductile plate segmentation may have further consequences,  
201 including for the stability of modern style subduction. In the Archean, higher mantle  
202 potential temperature<sup>14</sup> may have significantly reduced both plate strength and  
203 mantle resistance to slab penetration, and segmentation may have then induced  
204 frequent slab breakoff. This could have caused punctuated, episodic (intermittent)  
205 subduction<sup>15,16,17</sup>. Indeed, our numerical experiments performed even at modestly  
206 higher temperatures of 100-150 K larger than present-day show a strong tendency  
207 for slab disruption (Fig. 4a) and breakoff (Fig. 5a) in models with grain size  
208 reduction compared to those without (Figs. 4b, 5b). This may imply a sensitive  
209 dependence of subduction on mantle temperature, and thus possibly a larger role  
210 for an intermittent style of subduction in plate tectonics during our planet's  
211 cooling<sup>14</sup> compared to what is expected from mantle convection with memory-free  
212 rheologies. More generally, our models show that even oceanic lithosphere may be  
213 pervasively affected by deformation history, and the associated damage memory

214 affects not just surface deformation at trenches, but also how slabs deform and stir  
215 the surroundings during their descent to the lower mantle.

216

217

218

219

## 220 **References**

- 221 1. Ranero, C. R., Phipps Morgan, J. & Reichert, C. Bending-related faulting and  
222 mantle serpentinization at the Middle America trench. *Nature* 425, 367–373  
223 (2003).
- 224 2. Ranero, C.R., Sallarès, V. Geophysical evidence for hydration of the crust and  
225 mantle of the Nazca plate during bending at the north Chile trench. *Geology* 32,  
226 549–552 (2004).
- 227 3. Grevemeyer, I., Ranero, C.R., Flueh, E.R., Kläschen, D., Bialas, J. Passive and ac-  
228 tive seismological study of bending-related faulting and mantle serpentinization  
229 at the Middle America trench. *Earth Planet. Sci. Lett.* 258, 528–542 (2007).
- 230 4. Faccenda, M., Burlini, L., Gerya, T.V., Mainprice, D. (2008) Fault-induced seismic  
231 anisotropy by hydration in subducting oceanic plates. *Nature*, 455, 1097-1101.
- 232 5. Faccenda, M., Gerya, T.V., Burlini, L. (2009) Deep slab hydration induced by  
233 bending related variations in tectonic pressure. *Nature Geoscience*, 2, 790-793.
- 234 6. Faccenda, M., Gerya, T.V., Mancktelow, N.S., Moresi, L. (2012) Fluid flow during  
235 slab unbending and dehydration: Implications for intermediate-depth  
236 seismicity, slab weakening and deep water recycling. *Geochemistry, Geophysics,*  
237 *Geosystems*, 13, Article Number: Q01010.
- 238 7. Van Avendonk, H.J.A., Holbrook, W.S., Lizarralde, D., Denyer, P. Structure and  
239 serpentinization of the subducting Cocos plate offshore Nicaragua and Costa  
240 Rica. *Geochem. Geophys. Geosyst.* 12, Q06009 (2011).
- 241 8. Nakamura, Y., Kodaira, S., Miura, S., Regalla, C., Takahashi, N. High-resolution  
242 seismic imaging in the Japan Trench axis area off Miyagi, northeastern Japan.  
243 *Geophys. Res. Lett.*, 40, 1713–1718 (2013).

- 244 9. Boston, B., Moore, G.F., Nakamura, Y., Kodaira, S. Outer-rise normal fault  
245 development and influence on near-trench décollement propagation along the  
246 Japan Trench, off Tohoku. *Earth, Planets and Space*, 66, 135 (2014).
- 247 10. Shillington, D. J. et al. Link between plate fabric, hydration and subduction zone  
248 seismicity in Alaska. *Nat. Geosci.* 8(12), 961–964 (2015).
- 249 11. Korenaga, J. On the extent of mantle hydration caused by plate bending. *Earth  
250 Planet. Sci. Let.* 457, 1-9 (2017).
- 251 12. Craig, T. J., Copley, A., Jackson, J. A reassessment of outer-rise seismicity and its  
252 implications for the mechanics of oceanic lithosphere. *Geophys. J. Int.* 197, 63–  
253 89 (2014).
- 254 13. Freed, A.M., Hashima, A., Becker, T.W. Okaya, D.A., Sato, H., Hatanaka, Y. (2017)  
255 Resolving depth-dependent subduction zone viscosity and afterslip from  
256 postseismic displacements following the 2011 Tohoku-oki, Japan earthquake.  
257 *Earth and Planetary Science Letters*, 459, 279-290.
- 258 14. Herzberg, C. et al. Thermal history of the Earth and its petrological expression.  
259 *Earth and Planet. Sci. Let.* 292, 79–88 (2010).
- 260 15. van Hunen, J., van den Berg, A. Plate tectonics on the early Earth: limitations  
261 imposed by strength and buoyancy of subducted lithosphere. *Lithos* 103, 217–  
262 235 (2008).
- 263 16. van Hunen, J., Moyen, J.-F. Archean subduction: fact or fiction? *Annual Review of  
264 Earth and Planetary Sciences* 40, 195–219 (2012).
- 265 17. Sizova, E., Gerya, T., Brown, M., Perchuk, L.L. Subduction styles in the  
266 Precambrian: Insight from numerical experiments, *Lithos*, 116, 209-229 (2010).
- 267 18. Zhong, S., Davies, G. F. Effects of plate and slab viscosities on the geoid. *Earth  
268 Planet. Sci. Let.* 170, 487–496 (1999).
- 269 19. Billen, M.I., Gurnis, M. Constraints on subducting plate strength within the  
270 Kermadec trench. *J. Geophys. Res.* 110, B05407 (2005).
- 271 20. Petersen, R.I., Stegman, D.R., Tackley, P.J. (2016) The subduction dichotomy of  
272 strong plates and weak slabs. *Solid Earth*, doi:10.5194/se-2016-56.

- 273 21. van Summeren, J., Conrad, C. P., Lithgow-Bertelloni, C. The importance of slab  
274 pull and a global asthenosphere to plate motions. *Geochem. Geophys. Geosys.*  
275 13, Q0AK03 (2012).
- 276 22. Garel, F., Goes, S., Davies, D. R., Davies, J. H., Kramer, S. C., Wilson, C. R.  
277 Interaction of subducted slabs with the mantle transition-zone: A regime  
278 diagram from 2-D thermo-mechanical models with a mobile trench and an  
279 overriding plate. *Geochem. Geophys. Geosys.* 15, 1739-1765, (2014).
- 280 23. Gerya, T.V., Connolly, J.A.D., Yuen, D.A. (2008) Why is terrestrial subduction one-  
281 sided? *Geology*, 36(1), 43-46.
- 282 24. Čížková, H., van Hunen, J., van den Berg, A.P., Vlaar, N.J. The influence of  
283 rheological weakening and yield stress on the interaction of slabs with the 670-  
284 km discontinuity, *Earth Planet. Sci. Lett.*, 199, 447-457 (2002).
- 285 25. Ribe, N. M. Bending mechanics and mode selection in free subduction: a thin-  
286 sheet analysis. *Geophys. J. Int.* 180,559-576 (2010).
- 287 26. Ghosh, A.; Becker, T. W.; Zhong, S. J. Effects of lateral viscosity variations on the  
288 geoid. *Geophys. Res. Lett.* 37 , L01301 (2010).
- 289 27. Karato, S., Wu, P. (1993) Rheology of the upper mantle: a synthesis. *Science* 260,  
290 771-778.
- 291 28. Ranalli, G. *Rheology of the Earth* (Chapman and Hall, 1995).
- 292 29. Mishin, Y.A., Gerya, T.V., Burg, J.-P., Connolly, J.A.D. Dynamics of double  
293 subduction: Numerical modeling. *Physics of the Earth and Planetary Interiors*,  
294 171, 280-295 (2008).
- 295 30. Funicello, F., Faccenna, C., Heuret, A., Lallemand, S., Di Giuseppe, E., Becker, T.  
296 W. Trench migration, net rotation and slab-mantle coupling. *Earth Planet. Sci.*  
297 *Lett.* 271, 233-240
- 298 31. Liu, L. and Stegman, D. R. (2011) Segmentation of the Farallon slab, *Earth and*  
299 *Planetary Science Letters*, 311, 1-10.
- 300 32. Gerya, T.V., Yuen, D.A. Robust characteristics method for modelling multiphase  
301 visco-elasto-plastic thermo-mechanical problems. *Phys. Earth Planet. Interiors*  
302 163, 83-105 (2007).

- 303 33. Bercovici, D., Ricard, Y. Mechanisms for the generation of plate tectonics by two-  
304 phase grain-damage and pinning. *Phys. Earth. Planet. Inter.* 202-203, 27–55  
305 (2012).
- 306 34. Bercovici, D., Ricard, Y. Plate tectonics, damage and inheritance. *Nature* 508,  
307 513–516 (2014).
- 308 35. Bercovici, D., Schubert, G., Ricard, Y. Abrupt tectonics and rapid slab detachment  
309 with grain damage. *Proceed. National Acad. Sci.* 112, 1287-1291 (2015).
- 310 36. Mulyukova, E., Bercovici, D. Formation of lithospheric shear zones: Effect of  
311 temperature on two-phase grain damage. *Phys. Earth Planet. Inter.* 270, 195–  
312 212 (2017).
- 313 37. Mulyukova, E., Bercovici, D. Collapse of passive margins by lithospheric damage  
314 and plunging grain size, *Earth. Planet. Sci. Lett.* 484, 341-352 (2018).
- 315 38. Mulyukova, E., Bercovici, D. The generation of of plate tectonics from grains to  
316 global scales: A brief review, for special “50th Annivesary of Plate Tectonics”  
317 volume of *Tectonics* 38, 4058–4076 (2019).
- 318 39. Gurnis, M., Hall, C., Lavier, L., Evolving force balance during incipient subduction.  
319 *Geochem. Geophys. Geosyst.* 5, Q07001 (2004).
- 320 40. Lavier, L.L., Buck, W.R., Poliakov, A.N.B. Factors controlling normal fault offset in  
321 an ideal brittle layer. *J. Geophys. Res.* 105, 23431–23442 (2000).
- 322 41. Choi, E., Lavier, L., Gurnis, M., Thermomechanics of mid-ocean ridge  
323 segmentation. *Phys. Earth Planet. Inter.* 171, 374–386 (2008).
- 324 42. Whitney, D.L., Teyssier, C., Rey, P., Buck, W.R. Continental and oceanic core  
325 complexes. *Geol. Soc. Am. Bulletin* 125, 273–298 (2013).
- 326 43. Hirauchi, K., Fukushima, K., Kido, M., Muto, J., Okamoto, A. Reaction-induced  
327 rheological weakening enables oceanic plate subduction. *Nat. Commun.* 7,  
328 12550 (2016).
- 329 44. Duretz, T. et al. The importance of structural softening for the evolution and  
330 architecture of passive margins. *Sci. Rep.* 6, 1-7 (2016)
- 331 45. John, T. et al. Generation of intermediate-depth earthquakes by self-localizing  
332 thermal runaway. *Nat. Geosci.* 2, 137-140 (2009).

- 333 46. Pozzi, G. et al. Coseismic ultramylonites: An investigation of nanoscale viscous  
334 flow and fault weakening during seismic slip. *Earth Planet. Sci. Let.* 516, 164-  
335 175 (2019).
- 336 47. Verberne, B.A. et al. Microscale cavitation as a mechanism for nucleating  
337 earthquakes at the base of the seismogenic zone. *Nat. Commun.* 8, 1645 (2017).
- 338 48. Dymkova, D., Gerya, T. Porous fluid flow enables oceanic subduction initiation  
339 on Earth. *Geophysical Research Letters*, 40, 5671–5676 (2013).
- 340 49. Brace, W. F., Kohlstedt, D. T. Limits on lithospheric stress imposed by laboratory  
341 experiments. *J. Geophys. Res.* 85, 6248–6252 (1980).
- 342 50. Byerlee, J. D. Friction of rocks. *Pure Applied Geophys.* 116, 615–626 (1978).

343

344

## 345 **Methods**

346 *Modeling approach.* The thermo-mechanical 2D numerical code I2VIS is used for the  
347 modeling of subduction initiation. It is based on a combination of a finite difference  
348 method, applied on a staggered Eulerian grid, and a marker-in-cell technique<sup>51,52</sup>. The  
349 momentum, mass and energy conservation equations are solved in an Eulerian frame, and  
350 physical properties are transported by Lagrangian. Non-Newtonian, visco-plastic  
351 rheologies and variable thermal conductivity are used in the model (Extended Data  
352 Table 1)<sup>27,28,53-57</sup>, which accounts for major phase transitions in the oceanic crust and  
353 mantle as well as adiabatic, radiogenic and frictional internal heating sources. Full details  
354 of this method, allowing for its reproduction, are provided elsewhere<sup>51,52</sup>.

355

356 *Numerical model design.* The initial model setup (Extended Data Fig. 1) corresponds to the  
357 one used for spontaneous subduction initiation at an oceanic transform fault<sup>23,39</sup>. The  
358 computational domain is equivalent to 3000 × 3000 km (Extended Data Fig. 1) and is  
359 resolved with an irregular rectangular grid of 1261 × 511 nodes and contains 19 million  
360 randomly distributed markers. All sides of the model have free slip mechanical boundary  
361 conditions. The free surface boundary condition atop the crust is implemented by using a  
362 12 km thick “sticky” air/water layer<sup>58</sup> with low density (1 kg/m<sup>3</sup> above 9 km, 1000 kg/m<sup>3</sup>  
363 below 9 km) and viscosity (10<sup>17</sup> Pa s). The initial thermal structure and thickness of the

364 plate (Extended Data Fig. 1) is defined by prescribing a laterally uniform cooling age and  
 365 respective geotherm<sup>54</sup> with 273 K at the surface and the mantle potential temperature of  
 366 1523-1823 K varied in different experiments (Extended Data Table 2). We explored two  
 367 types of model setups with different initial conditions. In models with free subducting plate,  
 368 within 500 km at the right model boundary the subducting plate age gradually decreases  
 369 toward 1000 yr that corresponds to weak mid-ocean ridge located at the boundary  
 370 (Extended Data Figure 1a). In models without with subducting plate attached to the right  
 371 model boundary, subducting plate age remains unchanged toward the boundary (Extended  
 372 Data Figure 1a). An adiabatic gradient of 0.5 K/km is initially prescribed in the  
 373 asthenospheric mantle (Extended Data Fig. 1). Within 500 km at the lower boundary  
 374 temperature increases linearly by 744 K to mimic the hot boundary layer at the core-mantle  
 375 boundary. Temperature-dependent thermal conductivity is used for the mantle and the crust  
 376 (Extended Data Table S1). The thermal boundary conditions are 273 K at the top, 3567-  
 377 3717 K (depending on the mantle potential temperature) at the bottom and zero heat flux  
 378 on two other sides of the model. In order to insure efficient heat transfer from the surface  
 379 of the crust, the temperature of the “sticky” air/water is kept constant at 273 K.  
 380 Gravitational acceleration of 9.81 m/s<sup>2</sup> has been used in the model.

381 The surface of the lithosphere evolves by erosion and sedimentation according  
 382 to the following Eulerian transport equation<sup>59</sup>,

$$383 \quad \frac{\partial z_{es}}{\partial t} = v_z - v_x \frac{\partial z_{es}}{\partial x} - v_s + v_e,$$

384 where  $x$  and  $z$  are horizontal and vertical coordinates, respectively,  $z_{es}$  is the vertical  
 385 position of the surface as a function of the horizontal distance  $x$ ,  $v_z$  and  $v_x$  are the  
 386 vertical and horizontal components of the material velocity vector at the surface,  
 387 and  $v_s$  and  $v_e$  are the sedimentation and erosion rates, respectively. The  
 388 sedimentation and erosion rates correspond to the following relations<sup>60</sup>,  
 389  $v_s = 0$  mm/yr,  $v_e = 0.3$  mm/yr, when  $z < 9$  km (the sea-level prescribed in the model),  
 390 and  $v_s = 0.03$  mm/yr,  $v_e = 0$ , when  $z > z_{sea}$ . The maximal surface slope for the  
 391 accumulated sedimentary prism is limited by 17°. Surface processes however play  
 392 relatively minor role for subduction dynamics and slab morphology in our

393 numerical experiments as follows from test runs without surface processes  
394 (Extended Data Table 2).

395

396 *Density model.* We use the extended Boussinesq approximation with  
397 incompressible continuity equation and variable density in the momentum and  
398 energy conservation equations. The density of rocks varies with pressure ( $P$ ) and  
399 temperature ( $T$ ) according to the equation,

$$400 \quad \rho_{P,T} = \rho_0 [1 - \alpha(T - T_0)] [1 + \beta(P - P_0)],$$

401 where  $\rho_0$  is the standard density at  $P_0 = 1$  MPa and  $T_0 = 298$  K, and  $\alpha = 2 \times 10^{-5}$  1/K  
402 and  $\beta = 4.5 \times 10^{-12}$  1/Pa are the coefficients of thermal expansion and compressibility,  
403 respectively (Extended Data Table 1).

404 Our models take into account the phase transformations of olivine into  
405 wadsleyite and ringwoodite<sup>61</sup> and into bridgmanite in the mantle<sup>62</sup>. Eclogitization of  
406 subducted basaltic and gabbroic crust is taken into account by linearly increasing  
407 the density of the crust with pressure from 0% to 16% in the  $P$ - $T$  region between  
408 the experimentally determined garnet-in and plagioclase-out phase transitions in  
409 basalt<sup>63</sup>. The physical parameters for each experiment are presented in Extended  
410 Data Table 2.

411

412 *Visco-plastic rheological model.* The viscous and brittle (plastic) properties (see Extended  
413 Data Table 1) are implemented via evaluation of the effective viscosity of the material. For  
414 the ductile rheology, the contributions from different flow laws such as dislocation and  
415 diffusion creep are taken into account by composite rheology for  $\eta_{ductile}$

$$416 \quad \frac{1}{\eta_{ductile}} = \frac{1}{\eta_{diff}} + \frac{1}{\eta_{disl}}, \quad (1)$$

417  $\eta_{diff}$  and  $\eta_{disl}$  are effective viscosities for diffusion and dislocation creep, respectively.

418 For the crust, constant grain size is assumed and  $\eta_{diff}$  and  $\eta_{disl}$  are computed as

$$419 \quad \eta_{diff} = \frac{A}{2\sigma_{cr}^{n-1}} \exp\left(\frac{E+PV}{RT}\right), \quad (2)$$

$$420 \quad \eta_{disl} = \frac{1}{2} A^{\frac{1}{n}} \exp\left(\frac{E+PV}{nRT}\right) \dot{\epsilon}_{II}^{\frac{1}{n}-1}, \quad (3)$$

421 where  $R$  is gas constant,  $P$  is pressure,  $T$  is temperature (in K),  $\dot{\epsilon}_{II} = \sqrt{1/2(\dot{\epsilon}_{ij})^2}$  is the  
 422 square root of the second invariant of the strain rate tensor,  $\sigma_{cr}$  is the assumed diffusion-  
 423 dislocation transition stress, and  $A$ ,  $E$ ,  $V$  and  $n$  are experimentally determined pre-  
 424 exponential factor, activation energy, activation volume and stress exponent of the viscous  
 425 creep, respectively (Extended Data Table 1), which stand for the material constant, the  
 426 activation energy, the activation volume and the stress exponent, respectively.

427

428 For the mantle, the ductile creep model also takes into account grain size reduction and  
 429 growth processes assisted by Zener pinning, and  $\eta_{diff}$  and  $\eta_{disl}$  are computed as<sup>33,36,64</sup>. The  
 430 rheology follows a composite law as in (1), wherein

431 
$$\eta_{diff} = \frac{1}{2} A_{diff} h^m \exp\left(\frac{E_{diff} + PV_{diff}}{RT}\right), \quad (4)$$

432 
$$\eta_{disl} = \frac{1}{2} A_{disl}^{\frac{1}{n}} \exp\left(\frac{E_{disl} + PV_{disl}}{nRT}\right) \dot{\epsilon}_{II}^{\frac{1}{n}-1}, \quad (5)$$

433 Where  $h$  is a mean grain size,  $m$  is grain size exponent. The interplay between diffusion  
 434 and dislocation creep is controlled by a grain-size evolution equation dependent on the  
 435 mechanical work and temperature. The grain size evolution model relies on several  
 436 assumptions:

- 437 (1) Mantle peridotite is assumed to be composed of two well-mixed phases: olivine and  
 438 pyroxene with a fixed volume fraction of 60% and 40%, respectively. These phases  
 439 are considered to have the same density and rheology.
- 440 (2) In both phases the relative motion is considered to be negligible and therefore their  
 441 velocity  $v$  is the same.
- 442 (3) It is assumed that the grain size distribution is close to a self-similar log-normal  
 443 distribution. Therefore, it always retains the same shape and its mean variance and  
 444 amplitude are fully characterized by a unique grain size.

445 We make the further assumption that the system is in a state known as *pinned state limit*<sup>33,35</sup>  
 446 wherein the grain size evolution is controlled by the pinning of phases by each other (i.e.  
 447 Zener pinning is dominant)<sup>33</sup>. In these conditions, the grain size is controlled by the  
 448 roughness  $r$  of the interface between the two phases. A relation between the mean grain  
 449 size  $h$  (sufficient to fully describe the system) and the roughness  $r$  is given by  $h = \frac{r}{\sqrt{n_g}}$ ,

450 where  $h_g \approx \frac{\pi}{2}$  for the phase volume fraction in our model<sup>35</sup>. The roughness evolution is  
 451 described by the following equations<sup>33,36,64,65</sup>

$$452 \quad \frac{dr}{dt} = \frac{\eta G_I}{qr^{(q-1)}} - \frac{f_I r^2}{\gamma I \eta} \Psi \quad (6)$$

$$453 \quad G_I = \frac{G_g}{G_{fac}} \frac{q}{p} r^{(q-p)}, \quad (7)$$

$$454 \quad G_g = A_g \exp\left(\frac{E_g + PV_g}{RT}\right), \quad (8)$$

$$455 \quad f_I = f_0 \exp\left(-2\left(\frac{T}{1000}\right)^{2.9}\right) \quad (9)$$

456 where  $G_I$  is interface coarsening,  $G_g$  is grain growth rate,  $G_{fac} = 100$  is grain growth rate  
 457 factor,  $q = 4$  is roughness coarsening exponent,  $p = 2$  is grain size coarsening exponent,  $f_I$   
 458 is damage at the given temperature  $T$ ,  $A_g = 2 \times 10^{(4-6p)}$  is pre-exponential factor,  $E_g = 3 \times 10^5$   
 459 is a grain-growth activation energy,  $V_g = V_{diff}$  is a grain-growth activation volume,  $f_I$  is the  
 460 fraction of mechanical work  $\Psi$  converted to interface damage resulting in grainsize  
 461 reduction;  $f_0 = 0.001$  is interface damage at 1000 K,  $\eta = 3\phi_{ol}\phi_{px}$  is interface area density  
 462 depending on the volume fractions of olivine ( $\phi_{ol} = 0.6$ ) and pyroxene ( $\phi_{px} = 0.4$ ) in the  
 463 mantle.

464 The ductile rheology is combined with a brittle (plastic) rheology to yield an effective  
 465 viscous-plastic rheology using the following upper limit for the ductile viscosity

$$466 \quad \eta_{ductile} \leq \frac{C + \mu P}{2\dot{\epsilon}_{II}}, \quad (4)$$

$$467 \quad \mu = \mu_0 - \gamma\mu_\gamma \text{ for } \gamma \leq \gamma_0 \text{ and } \mu = \mu_1 \text{ for } \gamma > \gamma_0,$$

$$468 \quad \gamma = \int \sqrt{\frac{1}{2}(\dot{\epsilon}_{ij(\text{plastic})})^2} dt,$$

469 where  $\mu$  is the internal friction coefficient, ( $\mu_0$  and  $\mu_1$  are the initial and final internal  
 470 friction coefficient, respectively, Extended Data Table 1),  $\mu_\gamma = (\mu_0 - \mu_1)/\gamma_0$  is the rate of  
 471 faults weakening with integrated plastic strain  $\gamma$  ( $\gamma_0$  is the upper strain limit for the fracture-  
 472 related weakening),  $C$  is the rock compressive strength at  $P = 0$  (Extended Data Table 1),  
 473  $t$  is time (s),  $\dot{\epsilon}_{ij(\text{plastic})}$  is the plastic strain rate tensor. It is also assumed that the mantle  
 474 inside outer rise normal faults that reached the upper strain limit ( $\gamma_0$ ) is serpentinized and  
 475 has the respective rheology (Extended Data Table 1).

476 **Data availability**

477 All input and output files, used in the numerical modelling and visualisation are available  
478 on request.

479 **Code availability**

480 The numerical modelling code I2VIS and MatLab codes used for visualisation will be  
481 made accessible upon the paper acceptance.

482

483 **Acknowledgements** This work was supported by SNF projects 200021\_182069 and  
484 200021\_192296 (to T.V.G.) and NSF EAR-1853856 (to T.W.B.). The simulations were  
485 performed on the ETH-Zurich Euler and Leonhard clusters.

486

487

488 **References of Methods**

489

- 490 51. Gerya, T.V., Yuen, D.A., Characteristics-based marker-in-cell method with  
491 conservative finite-differences schemes for modeling geological flows with strongly  
492 variable transport properties. *Phys. Earth Planet. Interiors*, 140, 293-318 (2003).
- 493 52. Gerya T.V. *Introduction to Numerical Geodynamic Modelling. Second edition.*  
494 (Cambridge Univ. Press, 2019).
- 495 53. Hofmeister, A. M. Mantle values of thermal conductivity and the geotherm from  
496 Phonon lifetimes. *Science*, 283, 1699–1706 (1999).
- 497 54. Turcotte, D. L. & Schubert, G. *Geodynamics* (Cambridge Univ. Press, 2002).
- 498 55. Clauser, C., Huenges, E. Thermal conductivity of rocks and minerals. In: Ahrens, T.J.  
499 (editor), *Rock Physics and Phase Relations*. AGU Reference Shelf 3. American  
500 Geophysical Union, Washington DC, pp. 105–126 (1995).
- 501 56. Hirth, G., Kohlstedt, D. Rheology of the upper mantle and the mantle wedge: a view  
502 from the experimentalists. In: Eiler, J. (Ed.), *Subduction Factor Monograph*, vol.138.  
503 American Geophysical Union, Washington, DC, pp. 83–105 (2003).
- 504 57. Hilaret, N., B. et al. High-pressure creep of serpentine, interseismic deformation, and  
505 initiation of subduction. *Science*, 318, 1910–1913 (2007).

- 506 58. Schmeling, H. *et al.* A benchmark comparison of spontaneous subduction models:  
507 Towards a free surface. *Phys. Earth Planet. Inter.* 171, 198-223 (2008).
- 508 59. Gerya, T.V., Yuen, D.A. Rayleigh-Taylor instabilities from hydration and melting  
509 propel "cold plumes" at subduction zones. *Earth and Planet Sci. Lett.*, 212, 47-62  
510 (2003).
- 511 60. Baitsch-Ghirardello, B., Gerya, T.V., Burg, J.-P. Geodynamic regimes of intra-  
512 oceanic subduction: Implications for arc extension vs. shortening processes.  
513 *Gondwana Res.* 25, 546–560 (2014).
- 514 61. Katsura, T., & Ito, E. The system Mg<sub>2</sub>SiO<sub>4</sub>-Fe<sub>2</sub>SiO<sub>4</sub> at high pressures and  
515 temperatures: Precise determination of stabilities of olivine, modified spinel, and  
516 spinel. *J. Geophys. Res.*, 94, 663-670 (1989).
- 517 62. Ito, E. *et al.* Negative pressure-temperature slopes for reactions forming MgSiO<sub>3</sub>  
518 perovskite from calorimetry. *Science* 2J9, 1275-1278 (1990).
- 519 63. Ito, K. & Kennedy, G.C. in *The Structure and Physical Properties of the Earth's Crust*  
520 (ed Heacock, J.G.) 303–314 (Geophysical Monograph Series 14, AGU, 1971).
- 521 64. Bercovici, D., Ricard, Y. Generation of plate tectonics with two-phase grain-damage  
522 and pinning: Source-sink model and toroidal flow. *Earth Planet. Sci. Lett.* 365, 275–  
523 288 (2013).
- 524 65. Rozel, A., Ricard, Y., Bercovici, D. A thermodynamically self-consistent damage  
525 equation for grain size evolution during dynamic recrystallization. *Geophys. J. Int.*  
526 184, 719–728 (2011).

527

528 **Author Information.** The authors declare no competing financial interests.  
529 Correspondence and requests for materials should be addressed to T.G.  
530 ([taras.gerya@erdwethz.ch](mailto:taras.gerya@erdwethz.ch)).

531

## Figure legends

**Figure 1.** Dynamics of subduction and slab segmentation for 40 Ma old oceanic plate with 8 km thick crust formed under present day mantle temperature conditions (model xbeq, Extended Data Table S2). Left – evolution of viscosity structure. Right – evolution of grain size in the mantle. Left and right columns show evolution of viscosity structure and mantle grain size, respectively. Solid black lines indicate position of 1225°C isotherm.

**Figure 2.** Development of large-offset normal faults in the numerical model a, b (model xbeq, Extended Data Table S2, Fig. 1) and at the Japan trench<sup>9</sup> c, d. Solid black lines in a, b indicate position of 1225°C isotherm.

**Figure 3.** Influence of faults weakening and grain size evolution on subduction dynamics: a - model with both faults weakening and grain size evolution (model xbeqc, Extended Data Table S2), b - model with faults weakening but without grain size evolution (model xbeqca, Extended Data Table S2), c - model with grain size evolution but without faults weakening (model xbeqcb, Extended Data Table S2), d – with neither fault weakening nor grain size evolution (model xbeqcc, Extended Data Table S2). Mantle temperature is taken 100 K higher than present day values. Other parameters are the same as in the reference model (Fig. 1). Solid black lines indicate position of 1225°C isotherm.

**Figure 4.** Influence of model parameters on subduction dynamics in models with standard grain size evolution: a - failed subduction initiation in the model with 40 Ma subducting plate but without faults weakening (model xbeqab, Extended Data Table S2), b - no slab segmentation in the model with 40 Ma subducting plate but with 2.5 times slower rate of faults weakening with strain (model xbes, Extended Data Table

S2), c - reference slab segmentation model with 40 Ma subducting plate and standard faults weakening (model xbeq, Fig. 1, Extended Data Table S2), d – longer slab segments in the model with 100 Ma subducting plate and standard fault weakening (model xber, Extended Data Table S2). Mantle temperature is taken at present day values. Other parameters are the same as in the reference model (Fig. 1). Solid black lines indicate position of 1225°C isotherm.

**Figure 5.** Comparison of subduction dynamics for the models with a (model xbeqd, Extended Data Table S2) and without b (model xbeqda, Extended Data Table S2) grain size evolution. Mantle temperature is taken 150 K higher than present day values. Other parameters are the same as in the reference model (Fig. 1). Solid black lines indicate position of 1225°C isotherm.

### **Extended Data figure legends**

**Extended Data Figure 1.** Initial conditions for two types of subduction models explored in this study. a – model setup with free subducting plate detached from the right model boundary; subducting plate age changes to 1000 yr linearly with the distance within 500 km at the right model boundary. b – model setup with subducting plate attached to the right model boundary; subducting plate age does not change toward the boundary. White lines with numbers are isotherms in °C.

# Figures

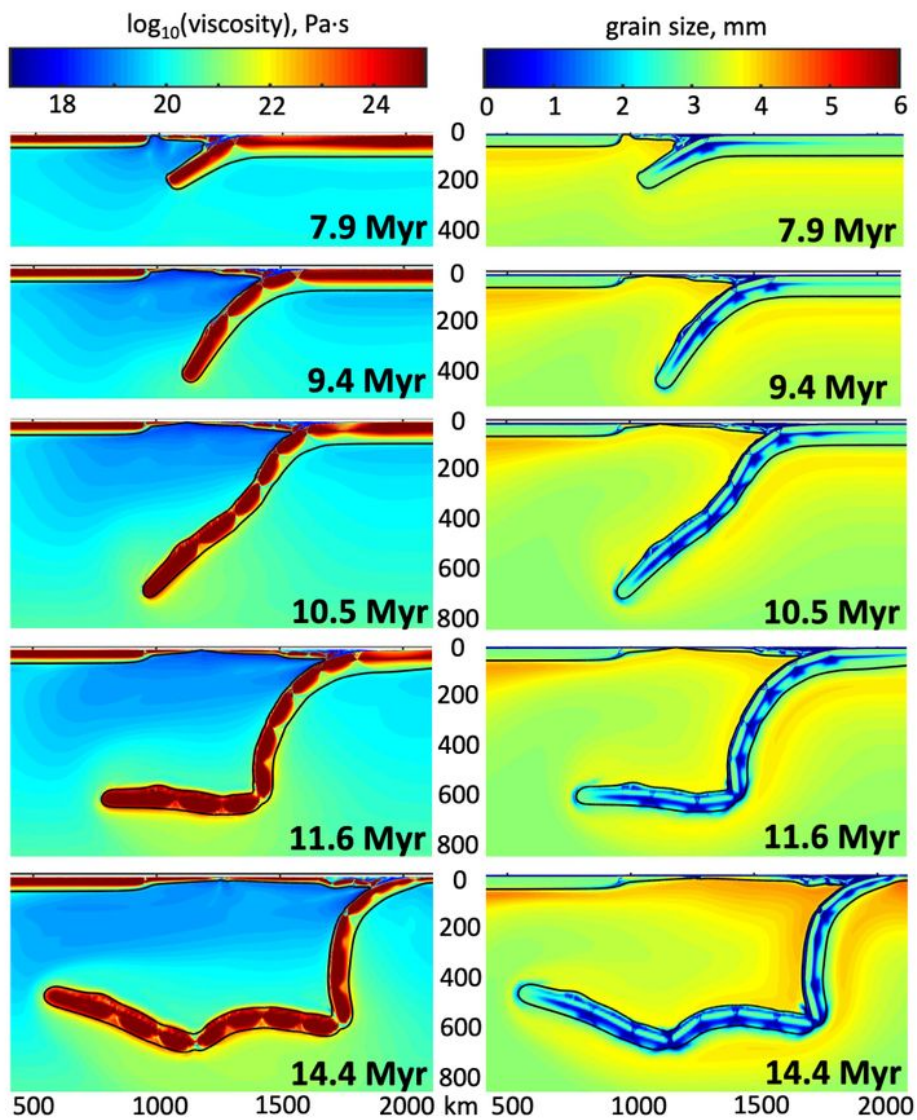
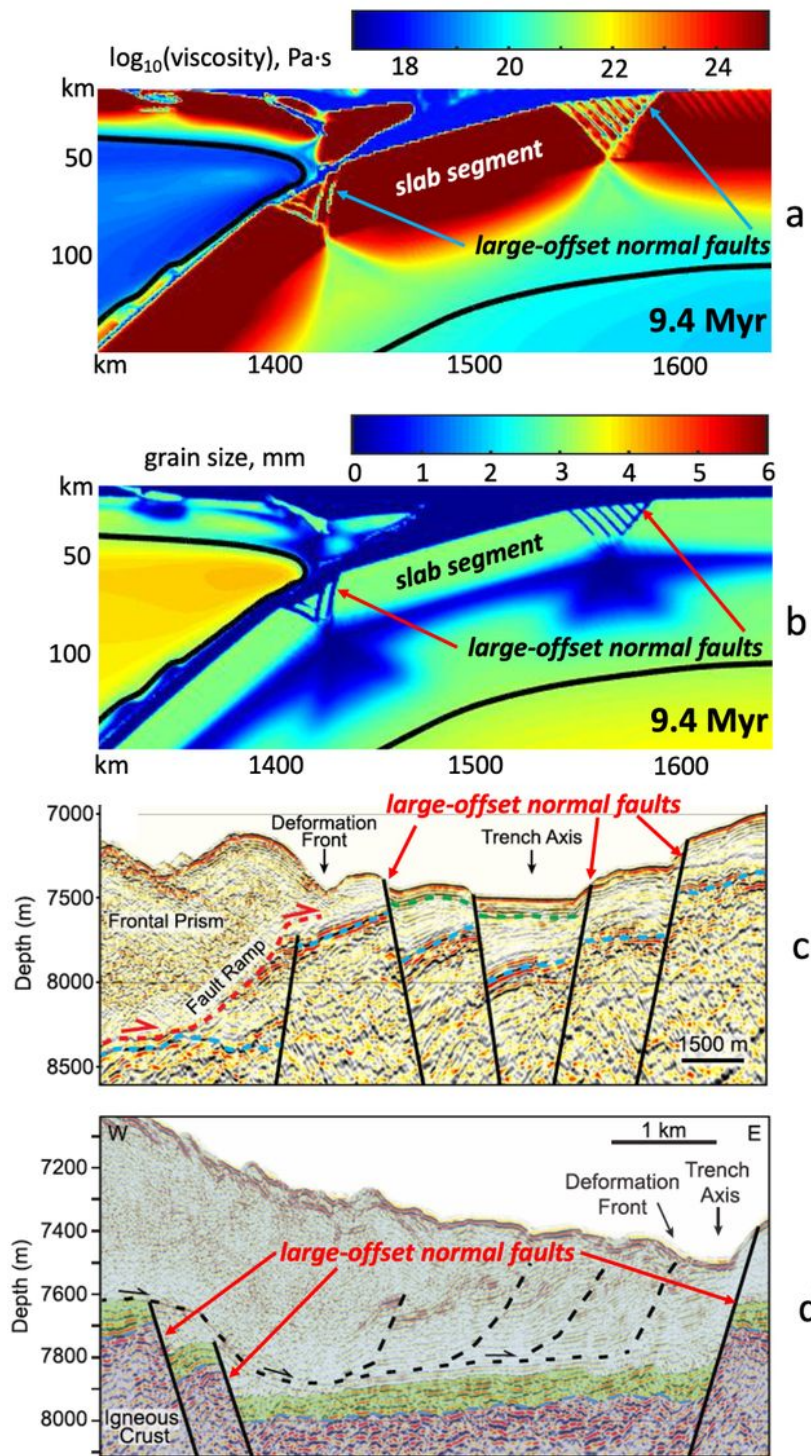


Figure 1

Dynamics of subduction and slab segmentation for 40 Ma old oceanic plate with 8 km thick crust formed under present day mantle temperature conditions (model xbeq, Extended Data Table S2). Left – evolution of viscosity structure. Right – evolution of grain size in the mantle. Left and right columns show evolution

of viscosity structure and mantle grain size, respectively. Solid black lines indicate position of 1225oC isotherm.



**Figure 2**

Development of large-offset normal faults in the numerical model a, b (model xbeq, Extended Data Table S2, Fig. 1) and at the Japan trench<sup>9</sup> c, d. Solid black lines in a, b indicate position of 1225oC isotherm.

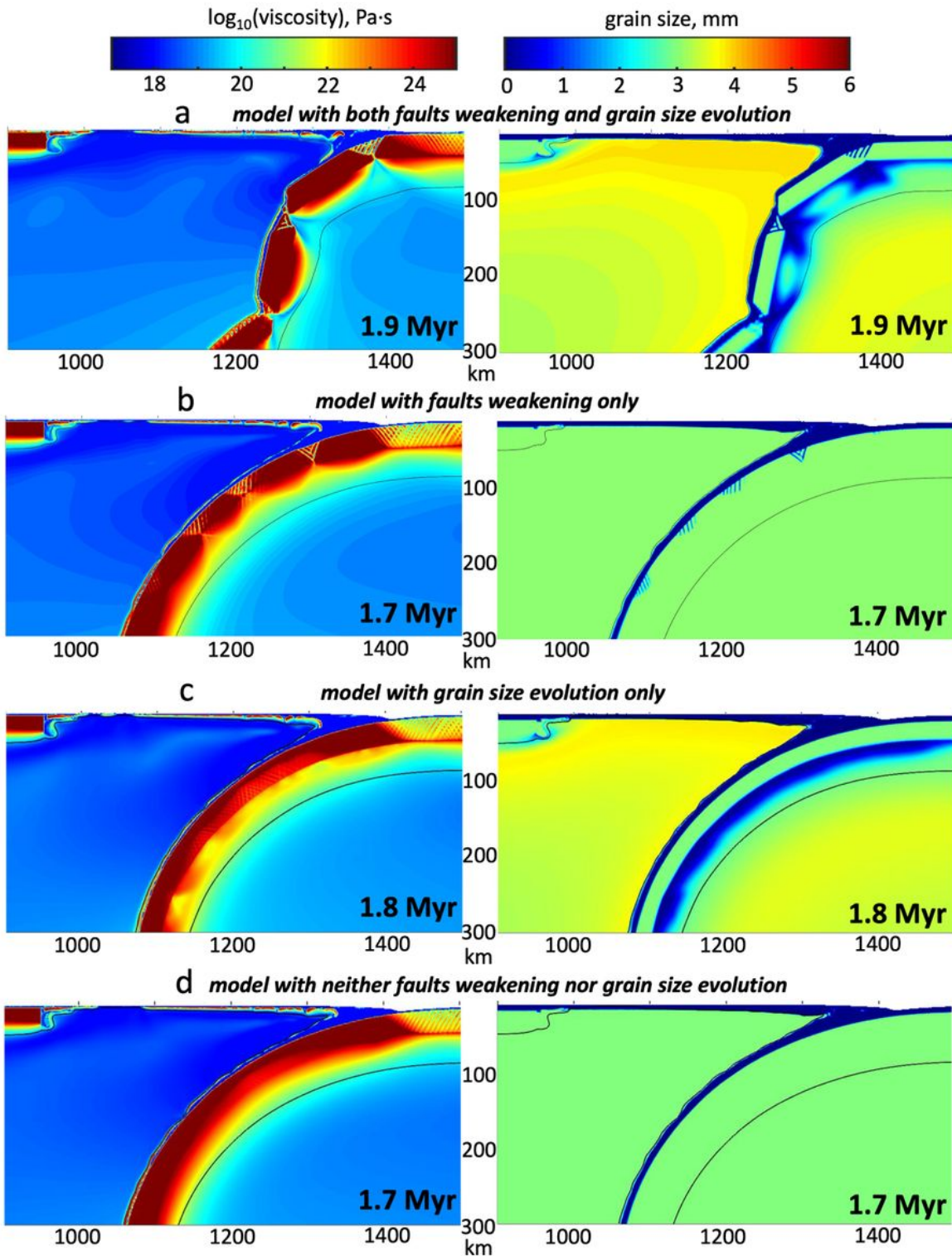


**Figure 3**

Influence of faults weakening and grain size evolution on subduction dynamics: a - model with both faults weakening and grain size evolution (model xbeqc, Extended Data Table S2), b - model with faults weakening but without grain size evolution (model xbeqca, Extended Data Table S2), c - model with grain size evolution but without faults weakening (model xbeqcb, Extended Data Table S2), d - with neither fault weakening nor grain size evolution (model xbeqcc, Extended Data Table S2). Mantle temperature is

taken 100 K higher than present day values. Other parameters are the same as in the reference model (Fig. 1). Solid black lines indicate position of 1225oC isotherm.

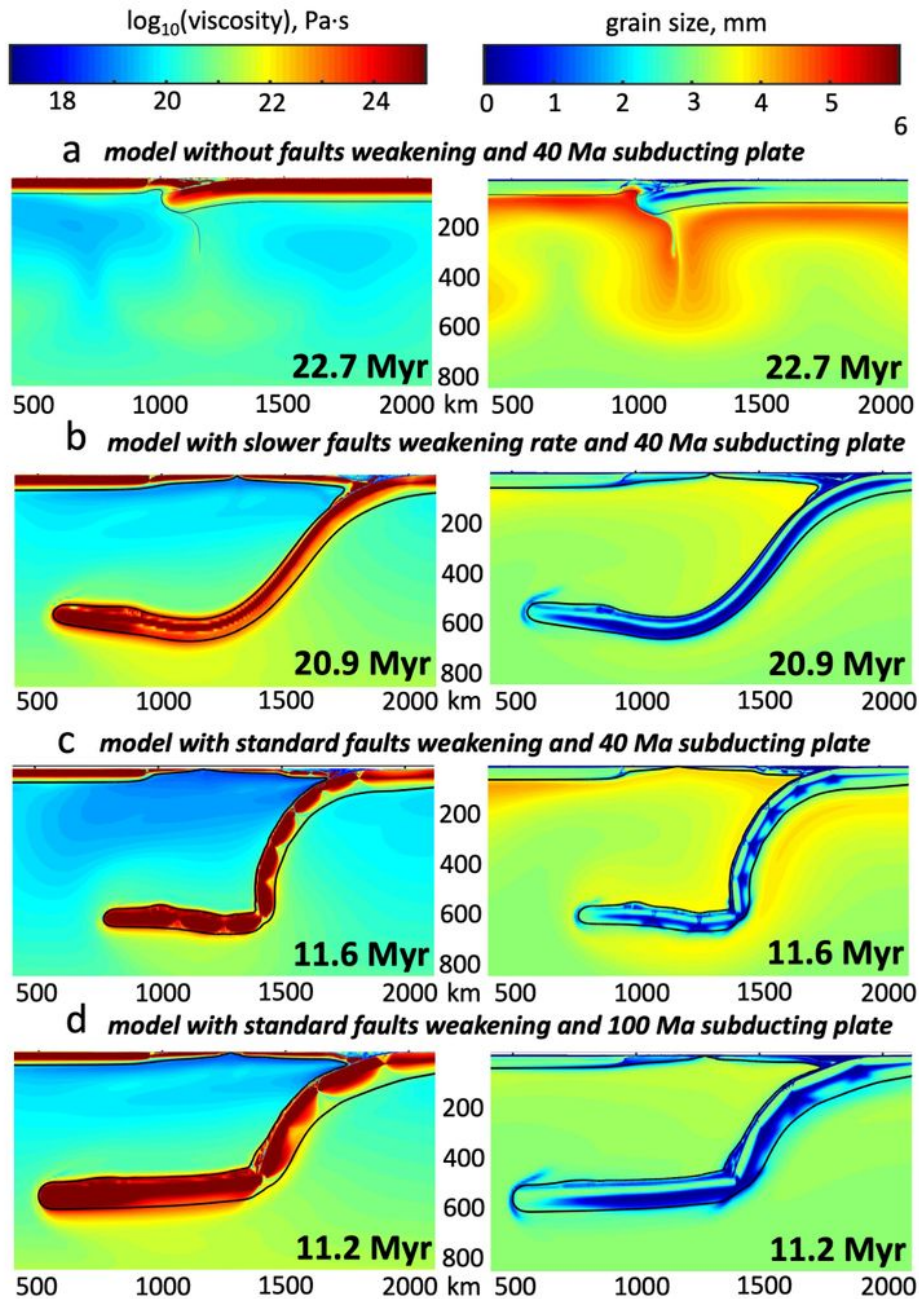


Figure 4

Influence of model parameters on subduction dynamics in models with standard grain size evolution: a - failed subduction initiation in the model with 40 Ma subducting plate but without faults weakening (model xbeqab, Extended Data Table S2), b - no slab segmentation in the model with 40 Ma subducting

plate but with 2.5 times slower rate of faults weakening with strain (model xbes, Extended Data Table S2), c - reference slab segmentation model with 40 Ma subducting plate and standard faults weakening (model xbeq, Fig. 1, Extended Data Table S2), d – longer slab segments in the model with 100 Ma subducting plate and standard fault weakening (model xber, Extended Data Table S2). Mantle temperature is taken at present day values. Other parameters are the same as in the reference model (Fig. 1). Solid black lines indicate position of 1225oC isotherm.

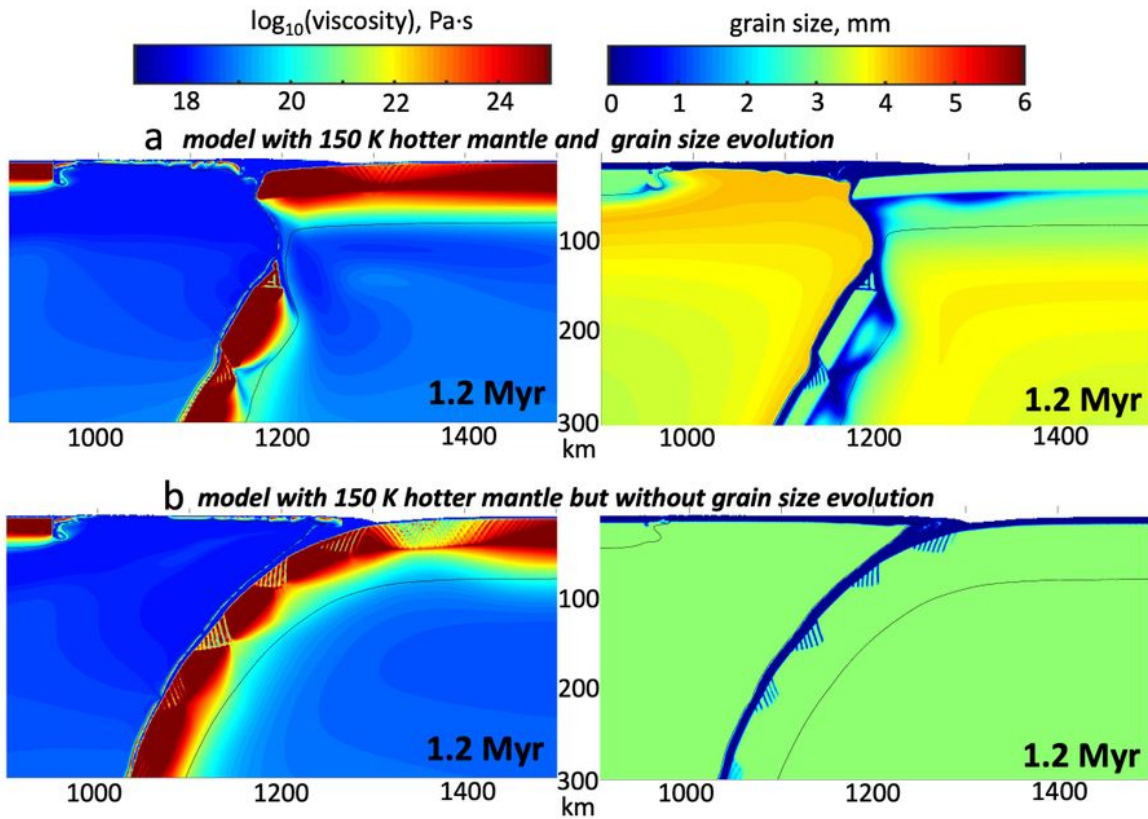


Figure 5

Comparison of subduction dynamics for the models with a (model xbeqd, Extended Data Table S2) and without b (model xbeqda, Extended Data Table S2) grain size evolution. Mantle temperature is taken 150 K higher than present day values. Other parameters are the same as in the reference model (Fig. 1). Solid black lines indicate position of 1225oC isotherm.

## Supplementary Files

This is a list of supplementary files associated with this preprint. Click to download.

- [ExtendedDataTable1.docx](#)
- [ExtendedDataTable2.docx](#)
- [ExtendedDataFigure1.jpg](#)